optica

Quantum cascade laser on silicon

Alexander Spott,[1,*] Jon Peters,[1] Michael L. Davenport,[1] Eric J. Stanton,[1] Charles D. Merritt,[2] William W. Bewley,[2] Igor Vurgaftman,[2] Chul Soo Kim,[2] Jerry R. Meyer,[2] Jeremy Kirch,[3] Luke J. Mawst,[3] Dan Botez,[3] and John E. Bowers[1]

[1]Department of Electrical and Computer Engineering, University of California, Santa Barbara, California 93106, USA
[2]Code 5613, Naval Research Laboratory, Washington, DC 20375, USA
[3]Department of Electrical and Computer Engineering, University of Wisconsin, Madison, Wisconsin 53706, USA
*Corresponding author: spott@ece.ucsb.edu

Received 29 February 2016; revised 13 April 2016; accepted 1 May 2016 (Doc. ID 260027); published 20 May 2016

The mid-infrared spectral region, 2–20 µm, is of great interest for sensing and detection applications, in part because the vibrational transition energies of numerous molecules fall in that region. Silicon photonics is a promising technology to address many of these applications on a single integrated, low-cost platform. Near-infrared light sources, heterogeneously integrated on silicon, have existed for more than a decade, and there have been numerous incorporations of mid-infrared optical devices on silicon platforms. However, no lasers fully integrated onto silicon have previously been demonstrated for wavelengths longer than 2.0 µm. Here we report, to the best of our knowledge, the first quantum cascade lasers on silicon emitting 4.8 µm light, integrated with silicon-on-nitride-on-insulator (SONOI) waveguides, and operating in pulsed mode at room temperature. The broadband and versatile nature of both quantum cascade lasers and the SONOI platform suggests that this development can be expanded to build photonic integrated circuits throughout the near- and mid-infrared on the same chip. © 2016 Optical Society of America

OCIS codes: (140.5965) Semiconductor lasers, quantum cascade; (130.0250) Optoelectronics; (140.3070) Infrared and far-infrared lasers; (130.3120) Integrated optics devices.

http://dx.doi.org/10.1364/OPTICA.3.000545

1. INTRODUCTION

The mid-infrared (MIR) regime promises to enable potentially transformative technologies. This spectral region includes absorption bands for molecules including H_2O, CH_4, CO_2, CO, NO_x, SO_x, NH_3, and many other chemicals and gases [1] that are important for medical, industrial, and military applications. MIR chemical bond spectroscopy of the earth's atmosphere and planetary bodies helps improve the understanding of greenhouse gases, pollutants, and biochemical compositions [2,3]. Tunable MIR diode lasers offer opportunities for high-resolution gas spectroscopic sensors and nonintrusive biochemical diagnostics [4–6]. Additionally, the atmospheric transmission windows in the 3–5 µm and 8–13 µm ranges can extend infrared technologies to longer distances for remote explosive detection, thermal imaging, and free-space communications [7,8].

Silicon integration offers the prospect of building inexpensive, compact devices that address these applications. A diverse portfolio of photonic sensors can potentially be integrated on a single silicon chip. In recent years there has been growing interest in integrated long-wavelength silicon devices; e.g., resonators [9], modulators [10], couplers [11], and multiplexers [12,13] have been demonstrated. Frequency combs, which can be used to build high-speed FT-IR spectrometers with no moving parts [14,15], have been shown spanning near- to mid-infrared wavelengths on silicon [16,17].

Heterogeneous integration by bonding III-V materials to silicon waveguides has enabled integrated detectors for wavelengths up to 2400 nm [18] and lasers on silicon from 1310 to 2010 nm [19]. Our previous demonstration of a 2010 nm heterogeneously integrated laser on silicon [20] utilized InGaAs quantum wells on an InP substrate. However, room-temperature InP-based type-I laser diodes have only been reported up to ~2.4 µm [21]. While InP-based type-II quantum wells have generated photoluminescence up to 3.9 µm, electrically pumped lasing has only been seen up to 2.6 µm [22]. GaSb-based type-I laser diodes can operate up to 3.6 µm [23].

Alternatively, the commercially available GaSb-based interband cascade laser (ICL) and InP-based quantum cascade laser (QCL) technologies provide promising potential for extending heterogeneous integration to wavelengths throughout the MIR. ICL ridges operate continuous-wave (CW) at room temperature from 2.9 to 5.7 µm with very low drive power [24], and emit up to 500 mW of CW power [25]. QCLs operate from 3 µm to the terahertz regime and can emit watts of CW output power [26,27]. The InP-based material system in QCLs is especially favorable for the complex fabrication processing necessary for heterogeneous silicon integration.

Although silicon-on-insulator (SOI) waveguides have been shown to have low loss at wavelengths out to 3.39 µm [28], the high material absorption of SiO_2 past ~3.6 µm demands

an alternative for longer wavelengths [29]. Silicon-based waveguide designs that have been suggested [30] or demonstrated include silicon-on-sapphire (SOS) [9], silicon-on-nitride (SON) [31], germanium-on-silicon [32–34], and chalcogenide-on-silicon [35]. These platforms each have a limited optical bandwidth defined by the material absorption ranges of the waveguide core and cladding. Certain applications, however, benefit from or require an ultrabroadband platform. One way to achieve this is to use a platform that supports multiple waveguide designs on a single chip.

The silicon-on-nitride-on-insulator (SONOI) platform consists of three layers on a silicon substrate: silicon on silicon nitride on silicon dioxide. In this arrangement, MIR waveguides that can potentially support light spanning 1.2–6.7 μm [30] are defined with a top silicon device layer and a silicon nitride under-layer. By etching off the top silicon layer, the silicon nitride can be used as a second waveguide device layer, clad by silicon dioxide, for shorter wavelengths spanning 350 nm to 3.5 μm. By heterogeneously integrating lasers and detectors on the SONOI platform with multiple die bonding [36], a single silicon chip can contain sources and devices for wavelengths spanning from the UV to the MIR [37].

Here we demonstrate QCLs heterogeneously integrated on silicon with the SONOI ultrabroadband waveguide platform. These QCLs emit 4.8 μm light at room temperature in pulsed operation.

2. DESIGN

The device layout is similar to that used previously to heterogeneously integrate III-V lasers emitting at 2010 nm [20]. A top-view optical microscope image of a fabricated laser is shown in Fig. 1(a). Each laser consists of a 4 mm long hybrid silicon-QCL active region coupled to passive silicon waveguide regions at each side. Tapered III-V mesas are designed to couple light between the hybrid silicon-QCL mode and a passive silicon waveguide mode. A Fabry–Perot cavity is then formed by uncoated, polished silicon waveguide facets, one of which is shown in the scanning electron microscope (SEM) image in Fig. 1(b). It should also be possible to obtain feedback from gratings (DFB or DBR) or loop mirrors, as we have done successfully at shorter wavelengths [38].

The QCL material was grown by metalorganic chemical vapor deposition (MOCVD) at U. Wisconsin, with 30 active stages having a design similar to that described in [39]. A low injector doping (estimated to be mid-10^{11} cm^{-2}) was used to provide a low threshold current density. The surrounding layers, modified for heterogeneous integration on silicon, are shown in Table 1. A thick top InP cladding separates the optical mode from the contact metal, while a thin InP bottom cladding keeps the active region close to the silicon for improved efficiency of the taper mode conversion.

Figure 1(c) shows a cross-sectional schematic of the hybrid silicon-QCL region for Devices A and B discussed below. The laser geometry is designed to support light in the transverse magnetic (TM) polarization emitted by QCLs. A simulation from FIMMWAVE of the fundamental TM mode (for $\lambda = 4.8$ μm), which is shared between the narrow silicon waveguide and the InP QCL ridge waveguide, is shown projected onto the active region cross section in the schematic. Mode solver simulations find the transverse confinement factor Γ_{xy} in the QCL active core, which

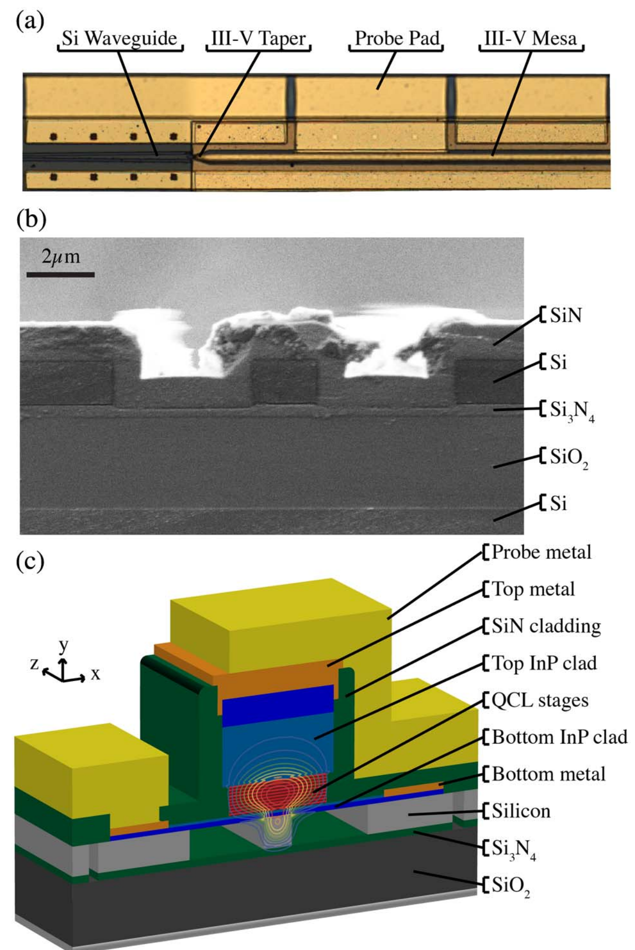

Fig. 1. (a) Optical microscope image of an integrated QCL. (b) Polished SONOI end-facet of an integrated QCL. (c) Cross-sectional schematic of a hybrid silicon-QCL active region. A contour plot of the electric field component, $|E_y|$, of the simulated fundamental TM optical mode is overlaid.

depends on both the III-V mesa and silicon waveguide widths, to be ≈0.76 and 0.73 for Devices A and B, respectively. The effective index of the mode is 2.97 in the passive SONOI region and 3.17 in the hybrid silicon-QCL active region.

The silicon waveguides are 1.5 μm tall, with a 400 nm Si_3N_4 lower cladding and a 3 μm buried SiO_2 layer. The III-V mesas for Devices A and B are 6 μm wide, and their silicon waveguides in the active region are 1 and 1.5 μm wide, respectively. Within the taper region, the III-V mesa linearly narrows from 6 μm wide to 500 nm wide at the taper tip, although the width of the fabricated taper tip varies from device to device. The silicon waveguide expands to 6 μm wide underneath the entire III-V taper region, and is 2 μm wide in the passive regions. The III-V taper lengths are 20 μm for Device A and 45 μm for Device B.

Two potential sources of internal loss for these devices are the optical overlap with both the 200 nm thick 1×10^{18} cm^{-3} doped n-InP bottom contact layer and the 3 μm thick SiO_2 cladding layer underneath the SONOI waveguide. Similar to the active region confinement, the confinement in the n-InP contact layer depends on the III-V mesa and silicon waveguide widths, and is found to be <0.04 for both devices. Although the free-carrier absorption in *n*-InP at this doping level and wavelength is not

Table 1. III-V Layers

Layers	Material	Thickness (nm)	Doping (cm-3)
Substrate	InP	–	–
Etch stop	InGaAs	50	–
Top contact	*n*-InP	1500	5×10^{18}
Top clad	*n*-InP	50	5×10^{17}
Top clad	*n*-InP	50	1×10^{17}
Top clad	*n*-InP	2450	2×10^{16}
Transition	*n*-InGaAs/InAlAs	50	1×10^{17}
Active core	*n*-QC structure	1510	Variable
Transition	*n*-InGaAs/InAlAs	50	1×10^{17}
Bottom clad	*n*-InP	50	1×10^{17}
Bottom clad	*n*-InP	50	5×10^{17}
Bottom contact	*n*-InP	200	1×10^{18}
Bonding SL	*n*-InP	7.5	1×10^{18}
Bonding SL	*n*-InGaAs	7.5	1×10^{18}
Bonding SL	*n*-InP	7.5	1×10^{18}
Bonding SL	*n*-InGaAs	7.5	1×10^{18}
Bonding layer	*n*-InP	10	1×10^{18}
Capping layer	*n*-InGaAs	200	1×10^{18}

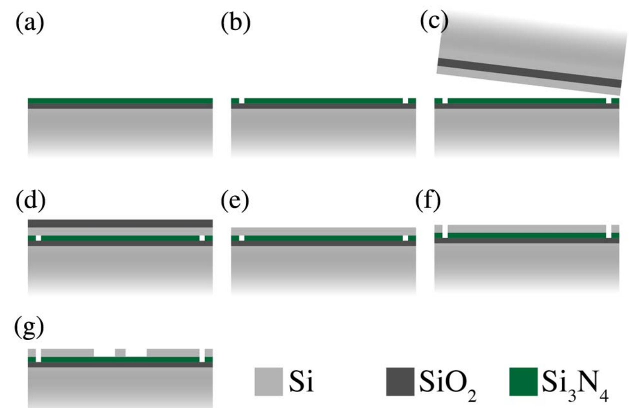

Fig. 2. Fabrication steps of the SONOI waveguides. (a) Begin with the NOI chip. (b) Dry etch the vertical outgassing channels through the Si_3N_4 and into the SiO_2. (c) Bond the SOI chip to the NOI chip. (d) Remove the Si substrate. (e) Remove the SiO_2 layer with buffered HF. (f) Dry etch the vertical outgassing channels in the Si device layer for later QCL bonding. (g) Dry etch the strip waveguides.

precisely known, we expect a loss contribution less than 1 cm^{-1} [40]. As with previous heterogeneously integrated lasers on silicon, the *n*-InP contact layer thickness and doping present a design trade-off between electrical performance, active core confinement, and internal loss that will be explored in future heterogeneously integrated QCL generations.

The overlap of the fundamental TM mode with the lower SiO_2 cladding was estimated by simulations to be 4.4×10^{-3} for the 2 μm wide passive SONOI waveguides, and $<3.4 \times 10^{-5}$ for the hybrid silicon-QCL active region of Devices A and B. This suggests a propagation loss contribution for the SiO_2 at 4.8 μm (using an estimated loss of 200 dB/cm [29]) of <1.0 dB/cm in the passive waveguide section and insignificant in the active region. A lower Si_3N_4 cladding thicker than 400 nm may be necessary to support extremely low-loss SONOI waveguides or lasers emitting at longer wavelengths where the SiO_2 absorption becomes higher. Leakage into the Si substrate is found to be negligible due to the sufficient SiO_2 thickness of 3 μm.

3. FABRICATION

The SONOI waveguide platform is constructed by transferring the device layer from a SOI wafer onto a nitride-on-insulator (NOI) wafer by direct wafer bonding. Each NOI wafer purchased from Rogue Valley Semiconductor consists of a silicon substrate with a 3 μm thermally grown SiO_2 layer and a 400 nm stoichiometric Si_3N_4 layer deposited on both top and bottom. The SOI wafer consists of a 1.5 μm Si device layer, a 1 μm buried SiO_2 (BOX) layer, and a Si substrate.

Figure 2 shows the process flow used to fabricate the SONOI waveguide. Vertical outgassing channels (VOCs) are etched through the Si_3N_4 and SiO_2 layers of the NOI chip. An SOI chip is then bonded after a plasma surface activation. The resulting chip is annealed in a graphite bonding fixture at 300 °C for 2 h, and then further annealed in a tube furnace at 900 °C for 4 h (with a 600 °C overnight idling). After bonding, the Si substrate is removed from the SOI chip by mechanical lapping and an inductively coupled plasma (ICP) $C_4F_8/SF_6/Ar$ etch, whose rate slows once it reaches the SiO_2. The SiO_2 layer is then removed with buffered HF to leave the SONOI chip. Finally, VOCs for QCL bonding and the strip waveguides are fully etched with $C_4F_8/SF_6/Ar$ ICP etches.

Figure 3 illustrates the QCL fabrication process. It begins by flip-chip bonding the QCL material to the SONOI chip after removing the capping layer (with an H_3PO_4:H_2O_2:DI 1:1:38 wet etch) and plasma activation. The InP substrate is removed by mechanical lapping and an HCl:DI 3:1 wet etch that selectively stops on an InGaAs etch stop layer.

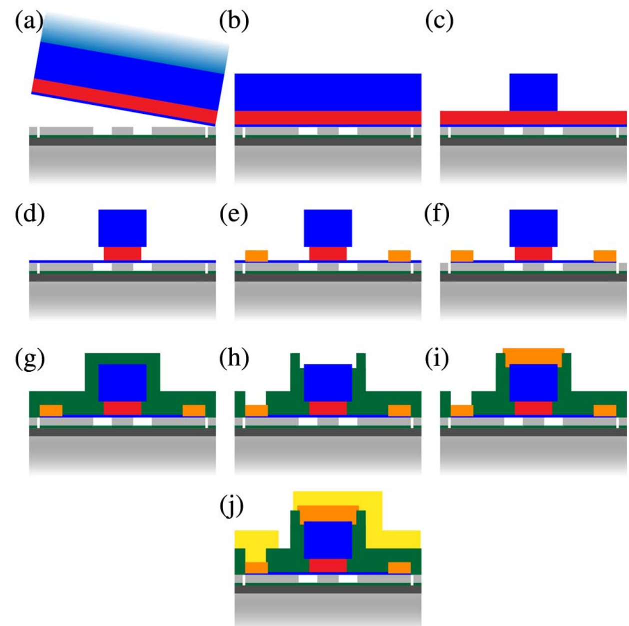

Fig. 3. Steps to fabricate integrated QCLs. (a) Bond the QCL material to the SONOI chip. (b) Remove the InP substrate. (c) Dry etch the top InP cladding. (d) Wet etch the QCL active stages. (e) Deposit n-metal for the bottom contact. (f) Dry etch the bottom InP cladding. (g) Deposit a SiN cladding by PECVD. (h) Dry etch vias. (i) Deposit n-metal for the top contact. (j) Deposit the probe metal.

The QCL mesa is defined with an SiO_2 hard mask. The InP top cladding is etched with a $CH_4/H_2/Ar$ reactive ion etch (RIE) and stopped at the QCL active region with laser endpoint detection. The QCL active region is removed with an H_3PO_4:H_2O_2:DI 1∶5∶15 wet etch. In order to reduce undercutting of the QCL layers, this etch is performed in multiple steps consisting of repeated stripping and repatterning of the photoresist. Pd/Ge/Pd/Au (10/110/25/1000 nm) is deposited for both the top and bottom contacts. Before the bottom contact metal is deposited, the bottom cladding is etched with a short RIE to reveal the 200 nm, highly doped *n*-InP bottom contact layer. Transmission line measurements estimated the sheet resistance of this layer to be 60–70Ω/sq, suggesting that the total series resistance contribution of the lateral current travel on both sides of the mesa is less than 0.1Ω. 1200 nm PECVD SiN is deposited as an electrical isolation layer, and vias are etched prior to depositing the top contact and probe metals. Laser bars are diced from the chip, and the SONOI facets are mechanically polished.

4. RESULTS

After fabrication, the silicon laser bar substrate was bonded with GE varnish to a copper submount and the probe pads were contacted with wire bonds to inject current. The lasers were driven with a pulsed current source that produced 250 ns wide pulses at a 1 kHz repetition rate for all of the measurements. The light output was collected with an f/1 aspheric ZnSe lens and focused onto a fast room-temperature HgCdTe detector with an f/2 aspheric ZnSe lens. Digitized scope readings were averaged from 150 to 200 ns to measure the detector voltage. A direct calibration of the measured detector voltage was obtained by operating the device at 200 kHz and measuring the output with both the above described collection and detection, and also with a 25 mm diameter thermopile detector placed directly at the device output.

The L-I-V characteristics for operation in pulsed mode at room temperature were measured for 10 integrated QCLs of varying geometries. Despite quantitative variations, the results are generally consistent qualitatively. Figure 4 plots the characteristics of two of the better lasers at 20 °C. The threshold currents are 388 and 387 mA for Devices A and B, respectively, while the maximum output powers are 17 and 31 mW. The slope efficiency near threshold for Device A is 150 mW/A, while for Device B it is 170 mW/A. The maximum wall-plug efficiency for Device B (from one of the two uncoated SONOI facets) is 0.35%.

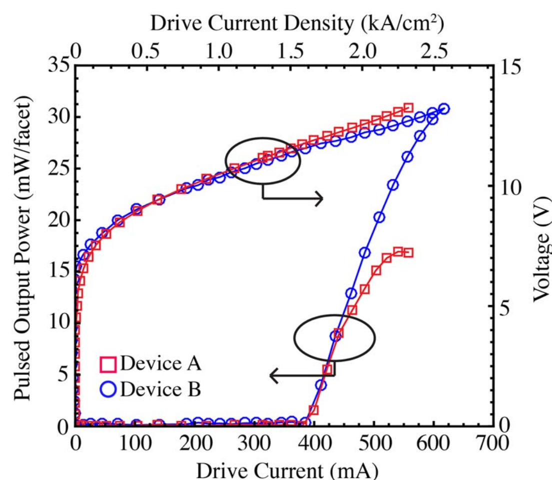

Fig. 4. Single-sided optical output power and voltage versus drive current of two integrated QCLs.

Figure 5(a) shows the output power emitted from Device A at a series of temperatures maintained by a thermoelectric cooler, ranging from 10 °C to 60 °C. Figure 5(b) plots the corresponding temperature dependence of the threshold current density obtained by dividing the threshold current by the III-V active area. The characteristic temperature T_0 was found to be 175 K by fitting the exponential function $J_{th} = J_0 \exp(T/T_0)$. This pulsed characteristic temperature is typical for a relatively low-injector-doping, 4.5–5.0 μm-emitting QCL [41] that is suitable for low-power-dissipation applications. A fit of the slope efficiency versus temperature yields $T_1 = 87$ K.

As with previous heterogeneously integrated lasers on silicon, the low thermal conductivity of the buried SiO_2 layer significantly impedes heat removal from the active region, while the GE varnish used to bond the laser bar to the copper submount introduces a further thermal barrier. However, poor heat dissipation is not a fundamental limitation. Possibilities for improvement include the introduction of a thermal shunt [42], or an epilayer-down arrangement wherein the top of the chip is bonded to a thermally conductive submount. Given the relatively low current and power density thresholds of these devices, along with their relatively high characteristic temperature, CW operation of the heterogeneously integrated QCLs at ambient temperature should be quite feasible.

Figure 6 shows the spectral emission from Device B at 20 °C. The spectrum acquired with a Digikrom 0.5 m monochromator with 1.5 nm resolution indicates a peak wavelength of 4.82 μm.

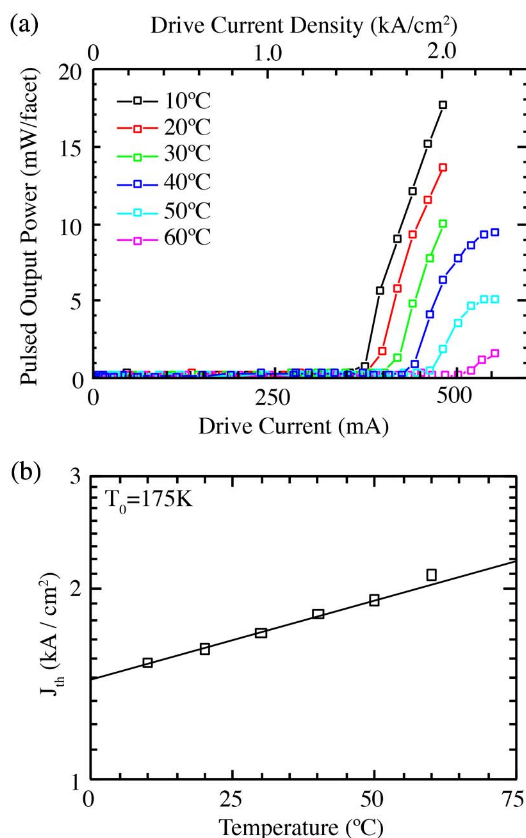

Fig. 5. (a) Single-sided output power versus drive current for Device A at temperatures from 10 °C to 60 °C. (b) Corresponding threshold current densities versus temperature. The fit yields a characteristic temperature of $T_0 = 175$ K.

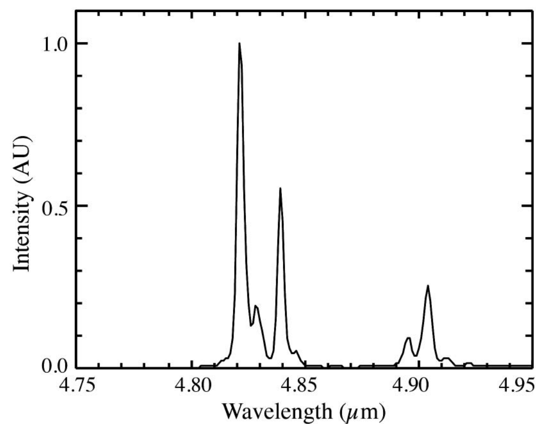

Fig. 6. Emission spectra of Device B measured with a monochromator at 20 °C.

The solid curves in Fig. 7 show horizontal (top) and vertical (bottom) far-field profiles of the emission from Device A. A similar profile along the slow axis was obtained for Device B (which was not measured along the fast axis). The dashed lines in the figures are FIMMWAVE simulations corresponding to the fundamental TM mode of the passive SONOI waveguides. That the measured profiles agree well with the simulated shapes, particularly in the horizontal direction, indicates that the QCLs emit primarily in the fundamental TM mode. The additional features at negative angles below ∼ – 15° along the fast axis are most likely due to polishing imperfections, such as residue on the SONOI facet or the surrounding cladding. According to the simulations, a higher-order transverse TM mode in the SONOI waveguide has strong optical overlap with the QCL core in the hybrid active region. Since that mode is expected to efficiently couple through the tapers into a higher-order mode in the passive silicon waveguide, the far-field measurements imply that this higher-order mode does not reach the lasing threshold.

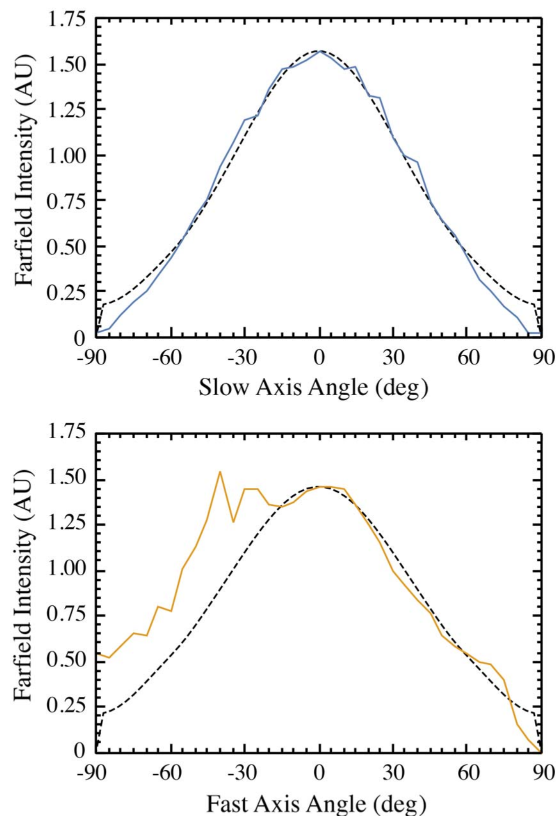

Fig. 7. Far-field intensity of Device A as a function of the angle normal to the facet in the slow (horizontal) axis (top) and fast (vertical) axis (bottom). Solid lines indicate measurements, and dotted lines indicate simulated profiles. Measurements were taken at 20 °C and a drive current of 500 mA.

A seemingly inconsistent feature of the L-I data shown in Figs. 4 and 5 is that while the threshold current densities for both devices are rather low (≈1.6 kA/cm^2), the single-facet slope efficiencies are also low (150–170 mW/A). This should not occur in a QCL, since a loss strong enough to suppress the efficiency by this amount should also substantially increase the lasing threshold. It suggests that strong feedback from the tapers, rather than the SONOI end-facets, may define the primary lasing cavity. A reduced efficiency then results from the smaller fraction of light generated within the higher-Q inner cavity (formed by the tapers) able to couple into the SONOI waveguide for extraction. In order to investigate this possibility, an antireflective (AR) coating was applied to the SONOI end-facets on the output side of some of the lasers. The AR coating deposited by electron beam evaporation consists of a $\lambda/4$ thick alumina layer (for $\lambda = 4.85$ μm) with refractive index ∼1.6. Figure 8 compares the L-I curves for Device A before (black) and after (red) the AR coating was applied. The threshold is seen to increase only modestly (by 20% to 466 mA) while the efficiency decreases from 153 to 89 mw/A (most likely because the threshold current is approaching the thermal rollover regime). Consistent results were obtained for one other device that showed a similar threshold increase and a slight increase of the efficiency. Three other devices did not lase following AR coating of the output facet, probably because they operated too close to the thermal rollover point. Device B had already been damaged when the AR coating experiments were performed.

The findings for the two devices that continued to lase following application of the AR coating are inconsistent with the assumption of lasing primarily within the cavity formed by the SONOI facets, since the much higher reflection loss at the AR-coated output facet should then have induced a proportionally larger increase of the lasing threshold. SEM inspection of the

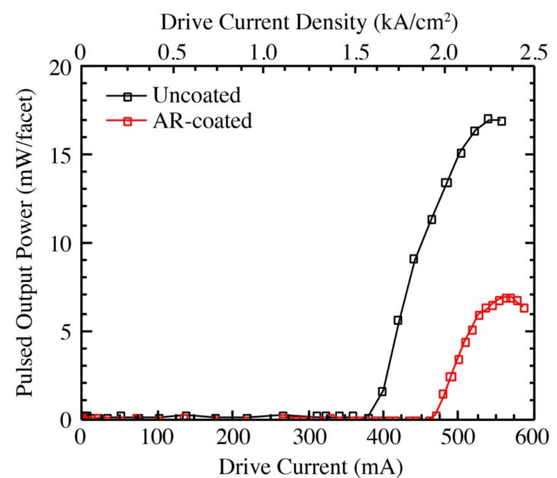

Fig. 8. Single-sided output power versus drive current at 20 °C for Device A before and after depositing an AR coating on the SONOI waveguide facets.

tapers during fabrication revealed substantial undercutting of the active region and a lithographic longitudinal misalignment between the upper cladding etch and the active region wet etch for some devices. The reflections within the taper were likely caused by the resulting active region taper, which was both non-uniform and shorter than the design. Variations of the fabricated taper tip geometry from device to device most likely produced different magnitudes of the taper reflectivities and transmission efficiencies. Such variations are probably responsible for the divergent performance characteristics of lasers that should have been more similar. Further experiments investigating the III-V taper dynamics will guide the optimization of future integrated QCL designs.

5. CONCLUSION

We have demonstrated the successful heterogeneous integration of QCLs on silicon with the broadband SONOI platform. Threshold currents as low as 387 mA and single-sided output powers as high as 31 mW are observed for pulsed operation at 20 °C. The observed characteristics imply that improved heat dissipation in future designs should enable CW lasing in the MIR. Furthermore, bonding materials from different QCL and/or ICL wafers will enable devices emitting at a wide range of wavelengths to be heterogeneously integrated on the same silicon chip.

Funding. Office of Naval Research (ONR) (N00014-13-C-0147); National Science Foundation (NSF) (DGE 1144085).

Acknowledgment. The authors thank Mijin Kim of Sotera Defense Solutions for useful discussions.

REFERENCES

1. L. S. Rothman, I. E. Gordon, Y. Babikov, A. Barbe, D. Chris Benner, P. F. Bernath, M. Birk, L. Bizzocchi, V. Boudon, L. R. Brown, A. Campargue, K. Chance, E. A. Cohen, L. H. Coudert, V. M. Devi, B. J. Drouin, A. Fayt, J.-M. Flaud, R. R. Gamache, J. J. Harrison, J.-M. Hartmann, C. Hill, J. T. Hodges, D. Jacquemart, A. Jolly, J. Lamouroux, R. J. Le Roy, G. Li, D. A. Long, O. M. Lyulin, C. J. Mackie, S. T. Massie, S. Mikhailenko, H. S. P. Müller, O. V. Naumenko, A. V. Nikitin, J. Orphal, V. Perevalov, A. Perrin, E. R. Polovtseva, C. Richard, M. A. H. Smith, E. Starikova, K. Sung, S. Tashkun, J. Tennyson, G. C. Toon, Vl. G. Tyuterev, and G. Wagner, "The HITRAN2012 molecular spectroscopic database," J. Quant. Spectrosc. Radiat. Transfer **130**, 4–50 (2013).
2. M. Gålfalk, G. Olofsson, P. Crill, and D. Bastviken, "Making methane visible," Nat. Clim. Change **6**, 426–430 (2016).
3. F. Pepe, D. Ehrenreich, and M. R. Meyer, "Instrumentation for the detection and characterization of exoplanets," Nature **513**, 358–366 (2014).
4. P. Werle, F. Slemr, K. Maurer, R. Kormann, R. Mücke, and B. Jänker, "Near- and mid-infrared laser-optical sensors for gas analysis," Opt. Lasers Eng. **37**, 101–114 (2002).
5. U. Willer, M. Saraji, A. Khorsandi, P. Geiser, and W. Schade, "Near–and mid-infrared laser monitoring of industrial processes, environment and security applications," Opt. Lasers Eng. **44**, 699–710 (2006).
6. E. Kerstel and L. Gianfrani, "Advances in laser-based isotope ratio measurements: selected applications," Appl. Phys. B **92**, 439–449 (2008).
7. C. Bauer, A. K. Sharma, U. Willer, J. Burgmeier, B. Braunschweig, W. Schade, S. Blaser, L. Hvozdara, A. Müller, and G. Holl, "Potentials and limits of mid-infrared laser spectroscopy for the detection of explosives," Appl. Phys. B **92**, 327–333 (2008).
8. J. W. Salisbury and D. M. D'Aria, "Emissivity of terrestrial materials in the 3–5 μm atmospheric window," Remote Sens. Environ. **47**, 345–361 (1994).
9. A. Spott, Y. Liu, T. Baehr-Jones, R. Ilic, and M. Hochberg, "Silicon waveguides and ring resonators at 5.5 μm," Appl. Phys. Lett. **97**, 213501 (2010).
10. L. Shen, N. Healy, C. J. Mitchell, J. S. Penades, M. Nedeljkovic, G. Z. Mashanovich, and A. C. Peacock, "Mid-infrared all-optical modulation in low-loss germanium-on-silicon waveguides," Opt. Lett. **40**, 268–271 (2015).
11. N. Hattasan, B. Kuyken, F. Leo, E. Ryckeboer, D. Vermeulen, and G. Roelkens, "High-efficiency SOI fiber-to-chip grating couplers and low-loss waveguides for the short-wave infrared," IEEE Photon. Technol. Lett. **24**, 1536–1538 (2012).
12. A. Malik, M. Muneeb, S. Pathak, Y. Shimura, J. Van Campenhout, R. Loo, and G. Roelkens, "Germanium-on-silicon mid-infrared arrayed waveguide grating multiplexers," IEEE Photon. Technol. Lett. **25**, 1805–1808 (2013).
13. A. Malik, M. Muneeb, Y. Shimura, J. V. Campenhout, R. Loo, and G. Roelkens, "Germanium-on-silicon planar concave grating wavelength (de)multiplexers in the mid-infrared," Appl. Phys. Lett. **103**, 161119 (2013).
14. A. Schliesser, N. Picqué, and T. W. Hänsch, "Mid-infrared frequency combs," Nat. Photonics **6**, 440–449 (2012).
15. F. Keilmann, C. Gohle, and R. Holzwarth, "Time-domain mid-infrared frequency-comb spectrometer," Opt. Lett. **29**, 1542–1544 (2004).
16. Y. Okawachi, K. Saha, J. S. Levy, Y. H. Wen, M. Lipson, and A. L. Gaeta, "Octave-spanning frequency comb generation in a silicon nitride chip," Opt. Lett. **36**, 3398–3400 (2011).
17. A. G. Griffith, R. K. W. Lau, J. Cardenas, Y. Okawachi, A. Mohanty, R. Fain, Y. H. D. Lee, M. Yu, C. T. Phare, C. B. Poitras, A. L. Gaeta, and M. Lipson, "Silicon-chip mid-infrared frequency comb generation," Nat. Commun. **6**, 6299 (2015).
18. R. Wang, S. Sprengel, M. Muneeb, G. Boehm, R. Baets, M.-C. Amann, and G. Roelkens, "2 μm wavelength range InP-based type-II quantum well photodiodes heterogeneously integrated on silicon photonic integrated circuits," Opt. Express **23**, 26834–26841 (2015).
19. H. Chang, A. W. Fang, M. N. Sysak, H. Park, R. Jones, O. Cohen, O. Raday, M. J. Paniccia, and J. E. Bowers, "1310 nm silicon evanescent laser," Opt. Express **15**, 11466–11471 (2007).
20. A. Spott, M. Davenport, J. Peters, J. Bovington, M. J. R. Heck, E. J. Stanton, I. Vurgaftman, J. R. Meyer, and J. Bowers, "Heterogeneously integrated 2.0 μm CW hybrid silicon lasers at room temperature," Opt. Lett. **40**, 1480–1483 (2015).
21. Y. Gu, Y. Zhang, Y. Cao, L. Zhou, X. Chen, H. Li, and S. Xi, "2.4 μm InP-based antimony-free triangular quantum well lasers in continuous-wave operation above room temperature," Appl. Phys. Express **7**, 032701 (2014).
22. S. Sprengel, C. Grasse, P. Wiecha, A. Andrejew, T. Gruendl, G. Boehm, R. Meyer, and M.-C. Amann, "InP-based Type-II quantum-well lasers and LEDs," IEEE J. Sel. Top. Quantum Electron. **19**, 1900909 (2013).
23. K. Vizbaras and M.-C. Amann, "3.6 μm GaSb-based type-I lasers with quinternary barriers, operating at room temperature," Electron. Lett. **47**, 980–981 (2011).
24. I. Vurgaftman, R. Weih, M. Kamp, J. R. Meyer, C. L. Canedy, C. S. Kim, M. Kim, W. W. Bewley, C. D. Merritt, J. Abell, and S. Höfling, "Interband cascade lasers," J. Phys. D **48**, 123001 (2015).
25. M. Kim, W. W. Bewley, C. L. Canedy, C. S. Kim, C. D. Merritt, J. Abell, I. Vurgaftman, and J. R. Meyer, "High-power continuous-wave interband cascade lasers with 10 active stages," Opt. Express **23**, 9664–9672 (2015).
26. Y. Bai, N. Bandyopadhyay, S. Tsao, S. Slivken, and M. Razeghi, "Room-temperature quantum cascade lasers with 27% wall plug efficiency," Appl. Phys. Lett. **98**, 181102 (2011).
27. Y. Yao, A. J. Hoffman, and C. F. Gmachl, "Mid-infrared quantum cascade lasers," Nat. Photonics **6**, 432–439 (2012).
28. G. Z. Mashanovich, M. M. Milošević, M. Nedeljkovic, N. Owens, B. Xiong, E. J. Teo, and Y. Hu, "Low loss silicon waveguides for the mid-infrared," Opt. Express **19**, 7112–7119 (2011).
29. E. D. Palik, *Handbook of Optical Constants of Solids* (Academic, 1998).
30. R. A. Soref, S. J. Emelett, and W. R. Buchwald, "Silicon waveguided components for the long-wave infrared region," J. Opt. A **8**, 840–848 (2006).
31. S. Khan, J. Chiles, J. Ma, and S. Fathpour, "Silicon-on-nitride waveguides for mid- and near-infrared integrated photonics," Appl. Phys. Lett. **102**, 121104 (2013).
32. Y.-C. Chang, V. Paeder, L. Hvozdara, J.-M. Hartmann, and H. Peter Herzig, "Low-loss germanium strip waveguides on silicon for the mid-infrared," Opt. Lett. **37**, 2883–2885 (2012).
33. M. Nedeljkovic, J. S. Penadés, C. J. Mitchell, A. Z. Khokhar, S. Stanković, T. D. Bucio, C. G. Littlejohns, F. Y. Gardes, and

G. Z. Mashanovich, “Surface-grating-coupled low-loss Ge-on-Si rib waveguides and multimode interferometers,” IEEE Photon. Technol. Lett. **27**, 1040–1043 (2015).
34. B. Troia, J. S. Penades, A. Z. Khokhar, M. Nedeljkovic, C. Alonso-Ramos, V. M. N. Passaro, and G. Z. Mashanovich, “Germanium-on-silicon Vernier-effect photonic microcavities for the mid-infrared,” Opt. Lett. **41**, 610–613 (2016).
35. H. Lin, L. Li, Y. Zou, S. Danto, J. D. Musgraves, K. Richardson, S. Kozacik, M. Murakowski, D. Prather, P. T. Lin, V. Singh, A. Agarwal, L. C. Kimerling, and J. Hu, “Demonstration of high-Q mid-infrared chalcogenide glass-on-silicon resonators,” Opt. Lett. **38**, 1470–1472 (2013).
36. H. Chang, Y. Kuo, R. Jones, A. Barkai, and J. E. Bowers, “Integrated hybrid silicon triplexer,” Opt. Express **18**, 23891–23899 (2010).
37. E. J. Stanton, M. J. R. Heck, J. Bovington, A. Spott, and J. E. Bowers, “Multi-octave spectral beam combiner on ultra-broadband photonic integrated circuit platform,” Opt. Express **23**, 11272–11283 (2015).
38. T. Komljenovic, S. Srinivasan, E. Norberg, M. Davenport, G. Fish, and J. E. Bowers, “Widely tunable narrow-linewidth monolithically integrated external-cavity semiconductor lasers,” IEEE J. Sel. Top. Quantum Electron. **21**, 214–222 (2015).
39. A. Evans, S. R. Darvish, S. Slivken, J. Nguyen, Y. Bai, and M. Razeghi, “Buried heterostructure quantum cascade lasers with high continuous-wave wall plug efficiency,” Appl. Phys. Lett. **91**, 071101 (2007).
40. O. K. Kim and W. A. Bonner, “Infrared reflectance and absorption of N-type InP,” J. Electron. Mater. **12**, 827–836 (1983).
41. D. Botez, C.-C. Chang, and L. J. Mawst, “Temperature sensitivity of the electro-optical characteristics for mid-infrared (λ = 3-16 μm)-emitting quantum cascade lasers,” J. Phys. D **49**, 043001 (2016).
42. M. N. Sysak, D. Liang, R. Jones, G. Kurczveil, M. Piels, M. Fiorentino, R. G. Beausoleil, and J. E. Bowers, “Hybrid silicon laser technology: a thermal perspective,” IEEE J. Sel. Top. Quantum Electron. **17**, 1490–1498 (2011).

128.111.50.109 {ts '2017-01-17 19:00:57'}